

See discussions, stats, and author profiles for this publication at: <https://www.researchgate.net/publication/272129525>

Critical role of silicon nanoparticles surface on lithium cell electrochemical performance analyzed by FTIR, Raman, EELS, XPS, NMR, and BDS spectroscopies

ARTICLE *in* THE JOURNAL OF PHYSICAL CHEMISTRY C · AUGUST 2014

Impact Factor: 4.77 · DOI: 10.1021/jp503949y

CITATIONS

8

READS

45

11 AUTHORS, INCLUDING:



Nicolas Dupré

French National Centre for Scientific Research

54 PUBLICATIONS 1,265 CITATIONS

[SEE PROFILE](#)



Philippe Moreau

Université de Nantes, CNRS

98 PUBLICATIONS 1,211 CITATIONS

[SEE PROFILE](#)



J.-S. Bridel

Umicore

11 PUBLICATIONS 251 CITATIONS

[SEE PROFILE](#)



Bernard Lestriez

Institut des Materiaux Jean Rouxel

124 PUBLICATIONS 1,540 CITATIONS

[SEE PROFILE](#)

Critical Role of Silicon Nanoparticles Surface on Lithium Cell Electrochemical Performance Analyzed by FTIR, Raman, EELS, XPS, NMR, and BDS Spectroscopies

N. Delpuech,^{†,‡} D. Mazouzi,[†] N. Dupré,^{†,§} P. Moreau,^{†,§} M. Cerbelaud,^{†,§} J. S. Bridel,[‡] J.-C. Badot,^{§,||} E. De Vito,[⊥] D. Guyomard,^{†,§} B. Lestriez,^{*,†,§} and B. Humbert[†]

[†]Institut des Matériaux Jean Rouxel (IMN), Université de Nantes-CNRS, Nantes, France

[‡]Umicore Group Research & Development Kasteelstraat 7, Olen, Belgium

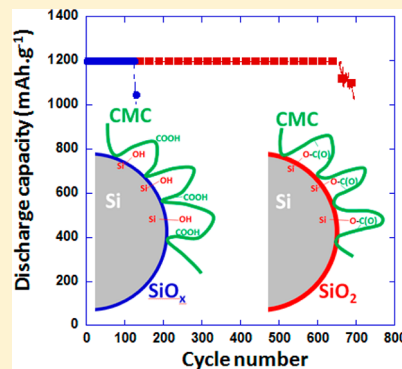
^{||}Laboratoire de Chimie de la Matière Condensée de Paris, CNRS, Chimie ParisTech, UPMC Univ Paris 06, Paris, France

[⊥]CEA, LITEN, Nanocharacterization Center, Minatec Campus, Grenoble, France

^{*}Réseau sur le Stockage Electrochimique de l'Energie (RS2E), FR CNRS, Nantes 3459, France

S Supporting Information

ABSTRACT: A pluri-disciplinary approach and a combination of techniques are used here to finely describe the surface of silicon nanoparticles used as active material in negative composite electrodes for lithium batteries. Although the surface of silicon particles is playing a major role in the electrochemical performance, it has rarely been characterized in depth. With respect to infrared analysis, we propose an analytical protocol, derived from the studies devoted to high specific area silica samples. Three different nanometric silicon powders are studied: a commercial one and two home synthesized silicon powders with specially designed surfaces. With respect to previous works and common belief, we demonstrate, on the electrochemical performance, a favorable effect of a particular thin layer silicon oxide with a well-defined SiO_2 composition at the extreme surface of the silicon particles.



INTRODUCTION

Rechargeable lithium-ion battery is one of the most promising energy storage technologies to enable a various range of clean transports (hybrid electric vehicles, electric vehicles, plug-in hybrid electric vehicles), which are essential to reduce the fossil oil dependency. In order to meet requirements of these automotive applications, it is necessary to find higher capacity electrode materials for Li-ion batteries. Providing new materials for the negative electrode of Li-ion cells has therefore been the subject of many investigations for more than a decade. As a result of such investigations, among the candidates for anode, silicon appears as an attractive alternative to graphite due to its natural abundance, high specific gravimetric capacity (3579 $\text{mAh}\cdot\text{g}^{-1}$ vs 372 $\text{mAh}\cdot\text{g}^{-1}$ for graphite), and a large volumetric capacity (2081 $\text{mAh}\cdot\text{cm}^{-3}$ vs 779 $\text{mAh}\cdot\text{cm}^{-3}$ by taking into account the volume variation). Silicon electrodes however suffer from poor cyclability due to the large volumetric expansion of silicon particles upon cycling.^{1,2} The successive swelling and shrinkage upon alloying/dealloying of the stack of silicon particles within the confined space of the electrochemical cell leads to major geometrical change of granular texture with a vast redistribution of interparticle contacts, the formation of cracks within the composite electrode and loss of electrical contacts at the current collector interface.^{3–6} The repetition of all these processes with frictional sliding of the

particles leads to a damaging of the SEI layer that exposes again the silicon particles surface to the liquid electrolyte. It results in an irreversible capacity loss at each cycle by the reduction at low potential of some liquid electrolyte on the exposed surface.^{2,7–9}

The surface of silicon particles is thus strongly involved in different phenomena of crucial importance for the electrochemical performance of lithium batteries with silicon-based composite electrodes. Silicon is always recovered by a native silicon oxide layer. Moreover, the silicon oxide layer is composed of hydroxylated terminations, the silanol (SiOH) groups, which likely dramatically increases the reactivity compared to the dehydroxylated siloxane phase ($\text{Si}-\text{O}-\text{Si}$).¹⁰

The nature of the interfacial bond (covalent or hydrogen) formed between silicon particle surfaces and the binder controls the mechanical strength of the granular structure. It also controls the ability of the granular structure to reversibly sustain the particles volume variations and displacements upon lithium uptake/release from silicon.^{11,12} Depending on the processing conditions, a covalent bond between silicon dioxide layer present at the surface of silicon particles and the

Received: April 23, 2014

Revised: June 21, 2014

Published: July 21, 2014



carboxylate function of the carboxymethyl cellulose binder (CMC) can occur,^{13–16} which results in stronger interparticle adhesion strength¹⁵ and longer cycle life.² Mazouzi et al.¹⁴ showed that the buffering of the slurry is mandatory to promote esterification (Si-OCO-R) between SiOH surface groups from the silicon oxide and the COOH functional groups of the CMC binder. In another study, Ding et al.¹⁷ also emphasized the role played by the pH of the aqueous electrode slurry. Koo et al.¹⁶ favored the formation of Si-OCO-R bonds by using a blend of CMC and poly(acrylic acid) (PAAH) binders and thermal treatment.

Moreover, the silanol groups could play a major role in the liquid electrolyte degradation. As a matter of fact, the grafting of silane on SiOH to form Si-O-Si-R terminations at the surface (with R of the alkyl type) minimizes the electrolyte solution decomposition.^{18,19} Furthermore, Philippe et al.²⁰ demonstrated an electrochemical reduction of the SiO₂ surface layer occurs at the first cycle with the formation of lithium silicate, Li₄SiO₄, and Li₂O as degradation products, as proven by X-ray photoelectron spectroscopy. As a consequence, various efforts^{21–23} have been made to reduce the thickness of silicon dioxide layer on silicon nanoparticles to decrease the first irreversible capacity and to enhance electrochemical performance. Many other investigations were also carried out in an attempt to further prevent the reactivity of the liquid electrolyte versus the surface of silicon-based materials. In this approach additives are mixed into the electrolyte. For instance, fluoroethylene carbonate (FEC) or/and vinylene carbonate (VC) that forms stretchable coating films upon polymerization at the silicon particle surface, create more stable solid electrolyte interphase (SEI).^{24–26}

Although the surface of silicon particles is playing a major role in the electrochemical performance, it has rarely been characterized in depth. A combination of techniques is here used to finely describe the surface of Si nanoparticles: diffuse reflectance infrared Fourier transform (DRIFT) spectroscopy combined with TGA, Raman spectroscopy, solid-state high-resolution nuclear magnetic resonance (MAS NMR), TEM coupled with electron energy loss spectroscopy (EELS), X-rays photoelectron spectroscopy (XPS), and finally broad band dielectric spectroscopy (BDS). With respect to infrared analysis, we propose an analytical protocol, derived from the studies devoted to high specific area silica samples. Diffuse reflectance spectroscopy allowed us to record infrared spectra of samples without any surface modification. Moreover, the near (NIR) and middle (MIR) infrared ranges are investigated. Since the NIR range corresponds to overtone or combination vibrational transitions, this area allows us to spectrally separate the vibrational modes of water molecule from the silanol modes. Then this spectral area is a useful tool in studying silanols groups without interference by water.

Three different nanometric silicon powders are studied: (i) a commercial one from Alpha Aesar Si_A, and two home synthesized silicon powders (ii) Si_U and (iii) Si_{Ud}. Si_{Ud} has a specially designed surface. With respect to previous works and common belief, we demonstrate, on the electrochemical performance, a favorable effect of a particular thin layer silicon oxide with a well-defined SiO₂ composition at its extreme surface.

EXPERIMENTAL METHODS

This study was carried out by using a commercial crystallized silicon powder from Alpha Aesar (sample Si_A) and two home

synthesized silicon powders: samples Si_U and Si_{Ud}. The method for making the Si_U powder comprises a step where a silicon precursor is vaporized in a gas stream at high temperature, after which the gas stream is quenched to obtain silicon nanoparticles. The silicon nanoparticles are then further quenched at low temperature in an oxygen containing gas.²⁷ Si_{Ud} was prepared from Si_U: a stirring stage in a HF solution for 10 min was followed by a washing sequence with ethanol to remove HF and a drying step at room temperature; then the dried powder was oxidized at 500 °C in air in a tubular furnace. Density analysis of the silicon powder is determined by He picnometry using an Accupyc 1330 picnometer.

For electrode preparation, Si_A, Si_U, or Si_{Ud} was used as the active material and Super P carbon black (noted CB, TIMCAL) as the conductive agent. Carboxymethyl cellulose (noted CMC, DS = 0.7, M_w = 90000, Aldrich) was used as binder. A total of 0.75 mL of pH = 3 buffer solution prepared with 24.6 mg of citric acid and 3.0 mg of KOH was added to a mixture of 160 mg of active material, 24 mg of CB, and 16 mg of CMC prior to ball-milling, using a silicon nitride vial and three silicon nitride balls.¹⁴ The slurry was tape-cast onto a copper foil, dried for 12 h at room temperature in air and 2 h at 100 °C in vacuum. It is important to note that citric acid and KOH from the buffer solution did not evaporate during the drying process and thus contribute to the mass of electrodes. Taking into account the volume of solution used, the Si/CB/CMC/(citric acid + KOH) wt % composition was 70.3/10.5/7.0/12.2.

Swagelok-type cells were used for the electrochemical tests, assembled in an argon-filled glovebox and cycled using a VMP automatic cycling/data recording system operating in a galvanostatic mode between 1 and 0.005 V versus Li⁺/Li⁰. The negative (which is also the reference electrode) was made of a disk of lithium metal. A borosilicate glass-fiber separator saturated with a 1 M LiPF₆ electrolyte solution (EC/DMC 1/1 or EC/DMC 1/1 with 10% of fluoroethylene carbonate (FEC) and 2% of vinylene carbonate (VC)). The cells were cycled with a limited discharge (lithiation-alloying) capacity of 1200 mAh·g⁻¹ of silicon at a rate of one lithium (de)inserted in Li_xSi in 2 h both in discharge and in charge, corresponding to a current density of 480 mA·g⁻¹ of silicon. The active mass loading was 0.9–1 mg cm⁻².

Diffuse Reflectance Infrared Spectroscopy. The chemical composition of the surface of the nanosized silicon was analyzed using infrared spectroscopy. The spectra were recorded in the diffuse reflectance mode with a vertex 70 Bruker spectrometer, in the medium and near-infrared ranges. We have recorded the diffuse reflectance with a Harrick HVC accessory. The silicon bulk is transparent in the middle infrared range due to the selection absorption rules. Only the phonon or vibrational modes implying dipolar variation will be displayed. So, only oxides at the interface of the silicon nanoparticles, Si—O—Si, SiOH, or Si—H groups are susceptible to possess infrared active vibrational modes in the middle infrared range. Consequently we have recorded the infrared spectra of samples without any mixing with another non-IR-absorbent matrix allowing us to avoid any surface modifications. A DTGS detector and a KBr beam splitter in the Michelson interferometer have been used for both spectral ranges NIR (8000–4000 cm⁻¹) and MIR (4000–400 cm⁻¹). For each sample, 1000 scans with a spectral resolution of 4 cm⁻¹ have been recorded. The sample spectra obtained by this technique are presented in this work as the result of the subtraction of the original spectrum and that of a reference. The pseudo

absorbance is plotted as $\log(R_{\text{sample}}/R_{\text{ref}})$, where R_{sample} and R_{ref} are, respectively, the diffuse single-beam reflectance of the sample and the reflectance reference.

Isotopic Exchange with D₂O. Silicon powder was put in D₂O saturated atmosphere during 12 h at room temperature in a glovebag. Diffuse reflectance was measured after isotopic exchange, as described in the previous section.

Raman Spectra. Spectra were recorded with a triple subtractive monochromator T64000 Jobin Yvon spectrometer equipped with an Olympus confocal microscope with a motorized 80 nm step XY stage. The detector was a charged coupled device (CCD) cooled by liquid nitrogen. The samples were excited with a laser beam at 488 or 514.53 nm emitted by an argon Laser (Spectra Physics). The details of the experimental setup are given elsewhere.²⁸ The laser beam with a power of about 400 to 600 μW was focused on samples with a diameter of about 0.8 μm . The Raman backscattering was collected through the objective of the microscope ($\times 100$, numerical aperture of 0.95) and dispersed by 1800 grooves-mm⁻¹ gratings to obtain 2.7 cm⁻¹ spectral resolutions for the 514.53 nm excitation beam. The wavenumber accuracy in vacuum was better than 0.8 cm⁻¹. The polarization discrimination of the optical device was checked by measuring the depolarization ratios for the perfectly known bands of reference liquid pure products. For instance, the experimental depolarization ratio for the 459 cm⁻¹ symmetric component of the CCl₄ spectrum is 0.02 ± 0.005 for the different wavenumber positions of the centered CCD camera or 0.03 ± 0.01 for the C–H stretching mode of CH₂Cl₂. In the case of our study, we have systematically checked the signal of a single crystal of silicon. The signal of the phonon T_g mode of this reference sample, was at 520.5 cm⁻¹ with a full width at half height of 2.8 cm⁻¹. It is interesting to note that the laser line at 488 nm enabled us to record a resonant Raman spectrum for Si crystallized nanopowder (nc-Si), whereas the 514 nm laser line available on the argon laser only revealed the phonon modes of the silicon substrate. This fact agrees with a higher band gap of nc-Si compared to bulk Si.²⁹ The laser irradiance was kept low (<1 kW·cm⁻²) to avoid any heating effect. We could rule out any heating effect by checking after a quite long period of laser irradiation (1–2 h), that the phonon mode at 520.5 cm⁻¹ of the bulk silicon substrate was not modified.

Thermogravimetric Analysis (TGA). Thermogravimetric analysis was performed on a PerkinElmer Model TGS-2 TGA system. Silicon powder was subjected to a thermal cycle at 5 °C·min⁻¹ from room temperature to 400 °C in a TG apparatus under argon. After TG measurement, the sample was analyzed by diffuse reflectance IR in order to obtain a relative infrared cross section and thus quantify of silanol concentrations, in all cases.

Electron Energy-Loss Spectroscopy (EELS). A Hitachi HF2000 TEM equipped with a Gatan 666 spectrometer, modified to include a CCD camera instead of a photodiode array, was used. Samples were directly deposited onto a holey carbon copper grid (no solvent used). In order to limit electron beam damage, the TEM was operated at 100 kV and a 5 nm probe size was used. Convergence and collection angles were 1.4 and 4.55 mrad, respectively. The energy resolution was approximately 0.8 eV and the energy dispersion was 0.08 eV per pixel. Total acquisition time was 10 s for the Si-L_{2,3} edge. All spectra were corrected for the gain and dark counts of the CCD camera. Deconvolution by the zero loss peak, recorded in

a hole of the TEM grid, was performed with the PEELS program.³⁰

X-ray Photoelectron Spectroscopy (XPS). The XPS spectra have been recorded on a SSI S-Probe XPS spectrometer. The X-ray source was an Al K α monochromatic beam (1486.6 eV). Data were collected at room temperature and the operating pressure in the analysis chamber was kept below 8×10^{-9} mbar. Pass energy was fixed at 25 eV, providing an energy resolution of ~730 meV. Data treatment was performed with CasaXPS software. After electrochemical cycling, electrodes were removed from the Swagelok cells, washed in DMC and transferred by using a specific transfer vessel, from the glovebox to the XPS fast entry load lock (FEL), without exposure to air. After the baseline (Shirley) was subtracted, the Si 2p curve fitting was performed using the non linear least-squares algorithms, assuming Gaussian peak shapes for each component. All spectra were calibrated taking C (sp²) as a reference binding energy of 284.5 eV.

Broad Band Dielectric Spectroscopy (BDS). Conductivity and permittivity spectra were recorded over a wide frequency range of 40–10¹⁰ Hz, using simultaneously an impedance analyzer Agilent 4294 (40 to 1.1×10^8 Hz), an impedance analyzer Agilent 4291 (10^6 to 1.8×10^9 Hz), and a network analyzer Agilent PNA E8364B (used from 10^6 to 10¹⁰ Hz). The experimental device, fully described in previous papers,^{31,32} is constituted by a coaxial cell in which the cylindrical sample with silver-plated front faces fills the gap between the inner conductor and a short circuit. Ag paste applied as a slurry and then dried provides a better contact with the sample than the use of metal foils. The sample has the same diameter (7 mm) as the outer conductor of the coaxial cell and a thickness between 0.5 and 1 mm. After an accurate calibration of the analyzers, complex permittivity $\epsilon(\omega) = \epsilon'(\omega) - i\epsilon''(\omega)$ and conductivity $\sigma(\omega) = i\omega\epsilon_0\epsilon(\omega)$ is computed from its admittance. Dielectric spectra were obtained with 600 measurements with a relative accuracy between 3 and 5%. Temperature-dependent measurements were made in an oven (293–380 K) and under dry N₂ flux (200–293 K).

Solid-State High-Resolution Nuclear Magnetic Resonance (NMR). Electrodes used for the ⁷Li MAS NMR were stopped at the end of charge. They were then removed from the current collector inside the glovebox and placed in cylindrical 2.5 nm diameter outside zirconia rotor without being washed but dried 12 h at room temperature on vacuum. ⁷Li MAS NMR experiments were carried out on a Bruker avance-500 spectrometer ($B_0 = 11.8$ T, Larmor Frequency ν_0 (⁷Li) = 194 MHz). MAS spectra were obtained by using a Bruker MAS probe. Spinning frequencies up to 25 kHz were used. ⁷Li NMR spectra were acquired with a single pulse sequence and a recycle time of 30 s. All the spectra were normalized taking into account the number of scans, the receiver gain, and the mass of the sample.

RESULTS AND DISCUSSION

Description of the Electrochemical Performance. Cycling life tests with capacity limitation of 1200 mAh·g⁻¹ of Si were carried out in order to compare the electrochemical performance of the three different silicon nanopowders (Si_U, Si_{UD}, and Si_A). Typical image of the silicon-based composite electrodes is shown in Figure S1 in the Supporting Information. By limiting the capacity to about 1/3 of the specific capacity of silicon (3579 mAh·g⁻¹), the volume variation of the Si particles is limited to 100% (rather than 270%), which allows a better

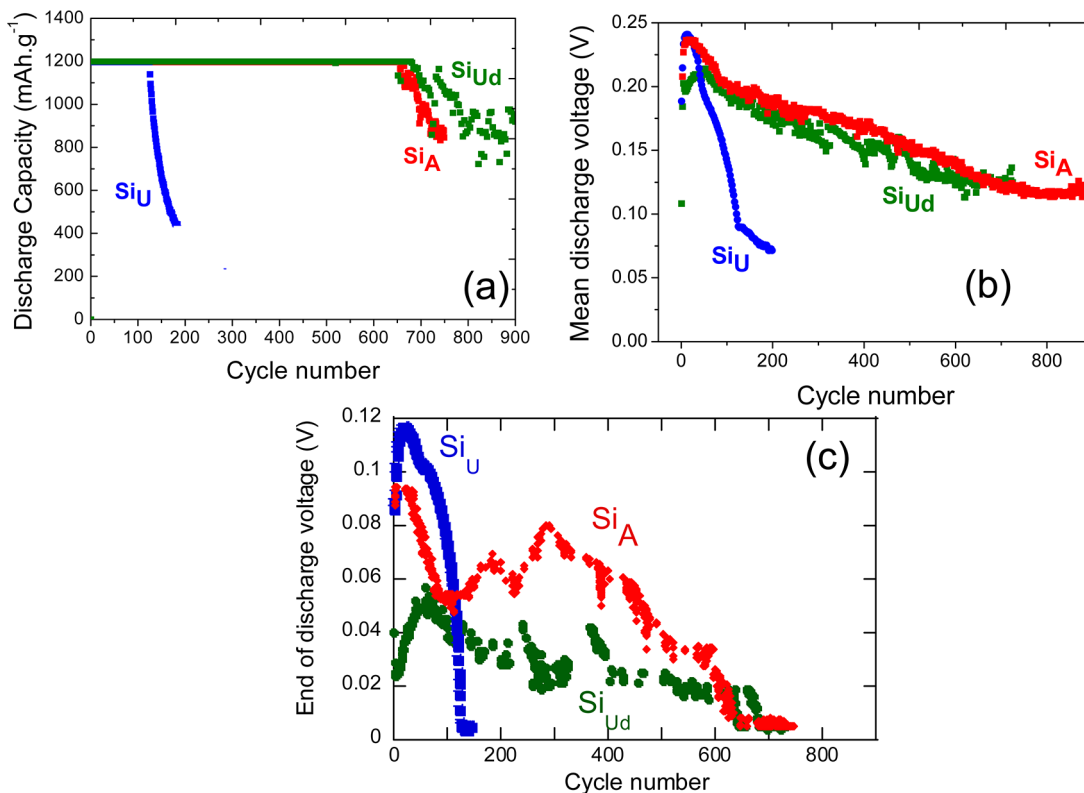


Figure 1. (a) Discharge capacity, (b) mean discharge voltage, and (c) end of discharge potential for Si_A (red), Si_U (blue), and Si_{Ud} (green).

reversibility and longer cycle life.¹⁴ The discharge capacity upon cycling is shown in Figure 1a. The cycle life decreases in the following order, Si_{Ud} ~ Si_A > Si_U with 680, 650, and 150 cycles, respectively. As already observed,^{8,14} the mean discharge voltage (Figure 1b) and the end of discharge voltage (Figure 1c) decrease upon cycling, after the activation period during which both initially increase. The capacity starts falling when the end of the discharge voltage reaches the potential cut off (0.005 V). The decrease of the mean and end of discharge voltages is due to three causes: (i) the electrical disconnection of the silicon particles as a consequence of their volume variations upon lithium alloying (dealloying) and the mechanical breakdown of the composite electrode architecture.^{3–5} (ii) The precipitation of the degradation products of the liquid electrolyte within the electrode porosity, which hinders the lithium ion diffusion toward the silicon particles.^{19,24} These two causes result in a rise of the electrode impedance. The third cause (iii) is the consequence of the two former causes: the loss of electronic (i) and ionic (ii) wiring decrease the number of silicon particles able to take part of the electrochemical reaction (lithium insertion/deinsertion). Thus, the remaining wired particles must form Li_xSi alloys with higher lithium content to sustain the 1200 mAh·g⁻¹ sought from the electrode. These lithium-rich alloys are formed at lower potential.

The clear variations in the cycle life between the different silicon powders are furthermore analyzed by comparing the Coulombic efficiencies (CE) and the incremental capacity curves. The Coulombic efficiency (expressed as a percentage) is the ratio (expressed as a percentage) between capacities removed from a battery during discharge and restored during charge. The main value of CE over the first 50 cycles decreases in the following order, Si_{Ud} ~ Si_A > Si_U in good correspondence

with the cycle life (Table 1). For Si_U, a lower first CE is observed and seems to be correlated with the poor cycle life.

Table 1. Coulombic Efficiency at the First Cycle and Mean Value of CE between the 2nd and 50th Cycle for Each Sample

sample	Coulombic efficiency (%)		irreversible loss (mAh/g)	
	1st cycle	mean value between 2nd and 50th cycle	1st cycle	mean value between 2nd and 50th cycle
Si _A	65 ± 1	99.0	420	12
Si _U	54 ± 1	97.7	546	28
Si _{Ud}	69 ± 1	99.0	372	12

This fact will be discussed in more details later. The typical evolution of incremental capacity curves is shown in Figure 2d–f. Two major steps (A and B) are observed as previously described.⁸ Peak A is ascribed to lithium poor alloys formation, whereas peak B is attributed to lithium rich alloys. At a capacity of 1200 mAh·g⁻¹, if all silicon particles are wired and thus can participate to the electrochemical reaction, only step A is observed (only lithium poor alloys are formed). On the contrary, if a large fraction of silicon particles are not anymore wired, the remaining wired particles must form lithium rich alloys and step B is observed. For all samples, at the first cycle, the two steps can be seen during the charge (delithiation), which shows the heterogeneous functioning of the composite electrode, the capacity being sought from only a fraction of the active mass. Such a heterogeneous functioning might be the consequence of a distribution in the wiring quality of the particles, some being well wired and others less well wired and less accessible to electrons and/or lithium ions. In general, after the activation period, one sees a homogenization of the

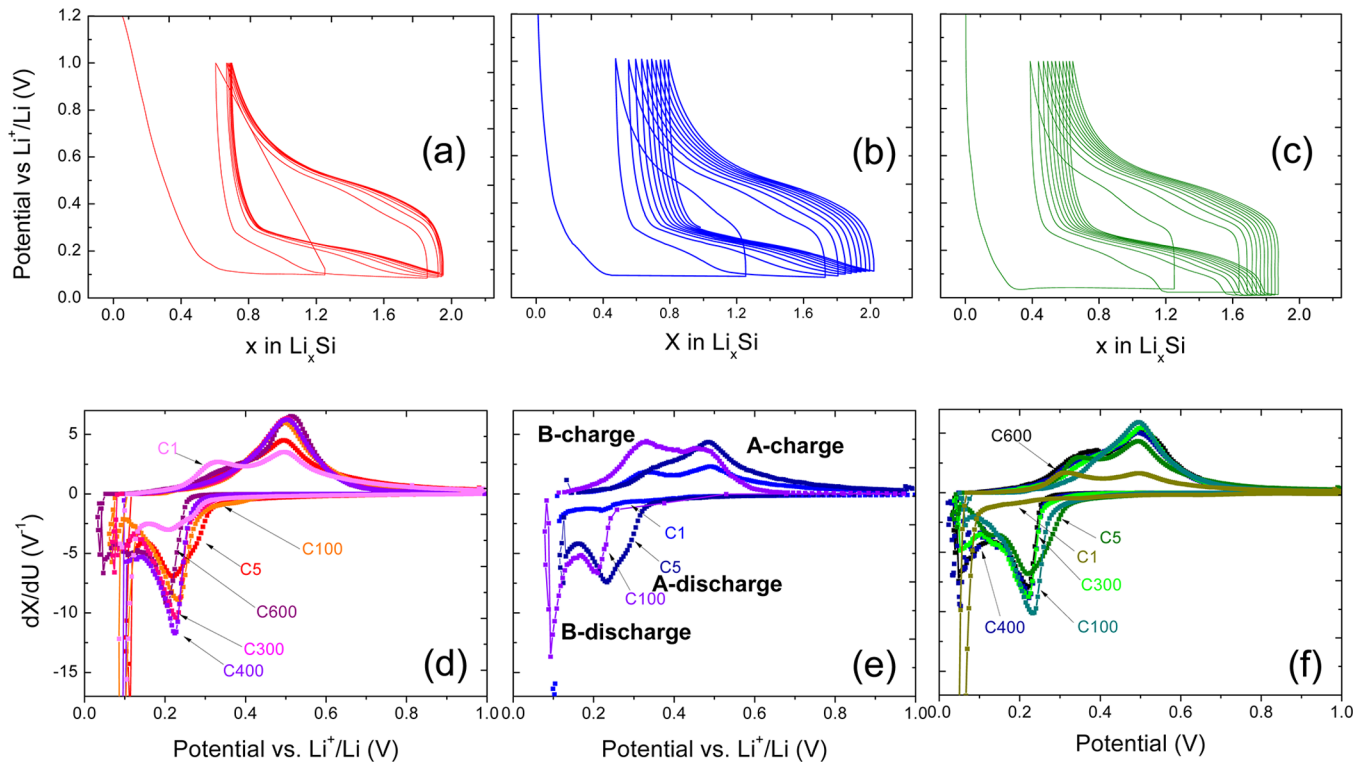


Figure 2. Voltage composition profile for (a) Si_{A} , (b) Si_{U} , and (c) Si_{Ud} . Incremental capacity curves for a selection of cycles for Si_{A} (d), Si_{U} (e), and Si_{Ud} (f).

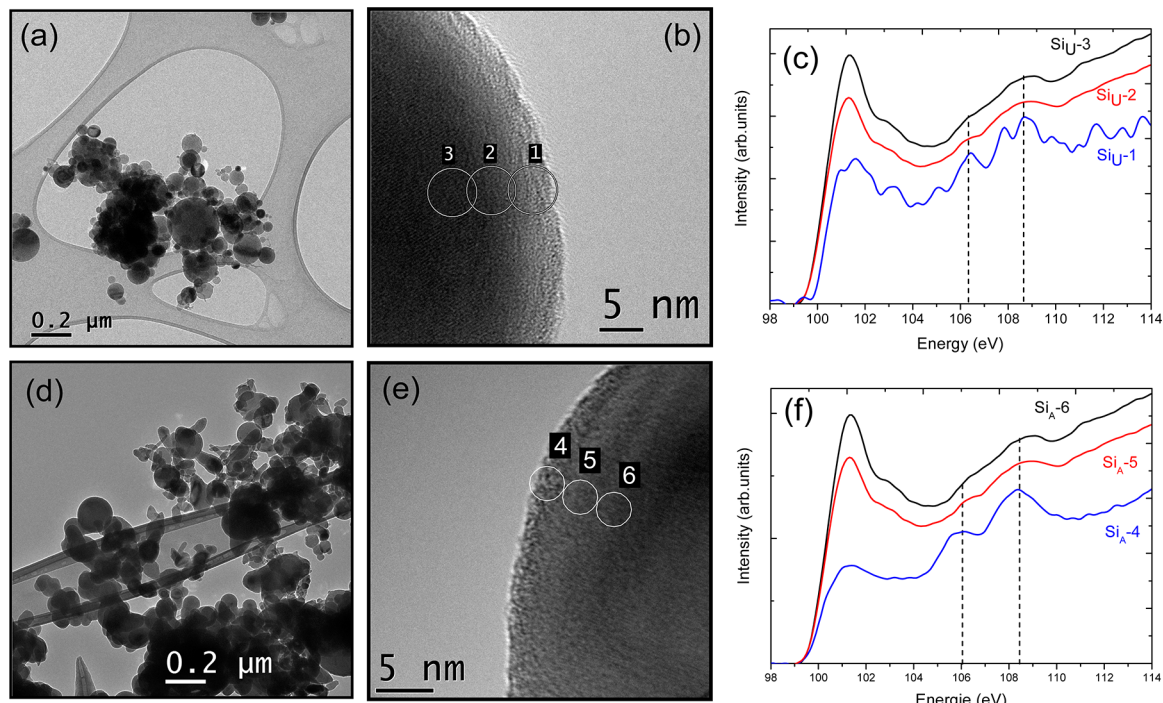


Figure 3. Transmission electron microscopy images obtained on the (a, b) Si_{U} and (d, e) Si_{A} samples. $\text{Si L}_{2,3}$ edge recorded point by point from silicon oxide surface to silicon bulk for (c) Si_{U} and (f) Si_{A} .

electrode functioning with the disappearance of step B. This is the case: at the fifth cycle the electrochemical activity mostly involves only step A for all silicon materials. Then, the intensity of step A is seen to decrease, while that one of step B increases, which reflects the decrease in the numbers of silicon particles able to participate to the electrochemical reaction as a

consequence of the wiring degradation. The decrease of step A is compensated by an increase of step B in order to provide the capacity required ($1200 \text{ mAh}\cdot\text{g}^{-1}$). However, this shift from step A only to step A plus step B in the electrochemical activity appears after different numbers of cycles, depending on the silicon material.

In the case of Si_{U} , the intensity of step B is already high after only 100 cycles. In the cases of Si_{Ud} and Si_{A} , the increase in step B intensity is, on the contrary, evidenced after a significantly higher number of cycles, 300 and 400, respectively. These observations are in agreement with the longer cycle life of the electrodes based on Si_{A} and Si_{Ud} compared to Si_{U} . This much higher reversibility of the Si_{A} and Si_{Ud} based electrodes could be attributed to less electrolyte degradation,⁹ as evidenced by the higher Coulombic efficiency, which could be due to better mechanical strength of the electrode^{2,33} or a lower reactivity at the interface between the nanoparticles and the electrolyte. In the following, the surface chemistry of the different silicon materials as well as their interaction with the CMC binder is studied.

Microscopic Description of the Surface Layers by TEM and EELS Spectroscopy and Raman Spectroscopy. The morphologies of the pristine silicon nanoparticles (Si_{A} and Si_{U}) were observed by using TEM (Figure 3a,b,d,e). Both samples are constituted of nanoparticles having a core–shell structure with a silicon core (Si^0) and a silicon oxide layer (a few nanometers). The Si_{U} layer is however thinner than that of Si_{A} . Complementary EELS spectra were recorded point by point from the surface to the bulk of the Si_{A} and Si_{U} particles (Figure 3c,f). At the extreme surface of the Si_{U} nanoparticles, EELS spectra consist of a first peak at 101 eV (onset 99.5 eV), which is assigned to Si^0 and a contribution of two peaks at 106.5 and 108.5 eV conventionally attributed to Si^{4+} in silicon dioxide, SiO_2 .^{34,35} The simultaneous presence of these three peaks suggests the presence of substoichiometric oxide SiO_x (with mean value of $x < 2$) at the extreme surface of Si_{U} . On the second spectra (2) taken more at the interior of the particle, the contribution from Si^{4+} becomes blurred and disappears entirely on the last spectra (3). Contrarily, the Si_{A} spectrum taken at the surface (4) shows the doublet (centered at 106 and 108 eV) but the intensity on the first peak at 101 eV is lower, indicating the presence of a thicker silicon oxide shell. We note that particle sizes range from 50 to 200 nm for both samples (Figure 3a,d), which could explain some inhomogeneity of EELS spectra. Careful analysis of high resolution TEM images show that the Si_{A} silicon oxide shell thickness is 2 nm.

Figure 4 displays Raman spectra of Si_{U} and Si_{A} at an excitation of 488 nm. For both samples, the full width at half-maximum of the symmetric lines of the T_g phonon of bulk silicon was around 4 cm⁻¹. No asymmetry was observed for both spectra. Then it is not necessary to consider any confinement of the phonon to interpret the Raman signal, that is, the bulk silicon appears to be formed by large enough crystals for the usual phonon signals to be obtained. In other words, there is no nanodomain of less than 10 nm in Si_{A} particles.²⁹ Complementary XRD diffraction patterns for Si_{A} and Si_{U} are compared in Figure S2 in the Supporting Information. Another observation is that only the spectrum of Si_{A} shows a small signal at around 496 cm⁻¹, that might be assigned to a highly hydroxylated phase of amorphous silica SiO_2 .³⁶ For Si_{U} , no signal in this spectral region emerged from the noise. Consistent with the TEM-EELS analysis, we can then deduce that relatively to the bulk silicon signal the silica phase is thinner for Si_{U} than for Si_{A} .

Influence of the Surface Layers on the Electrical Properties. Real parts of the conductivity of Si_{U} and Si_{Ud} are shown in Figure 5. Strong variations of the conductivity (increase of about 5 to 6 orders of magnitude) are shown versus frequency, as generally observed.^{37–41} The high-

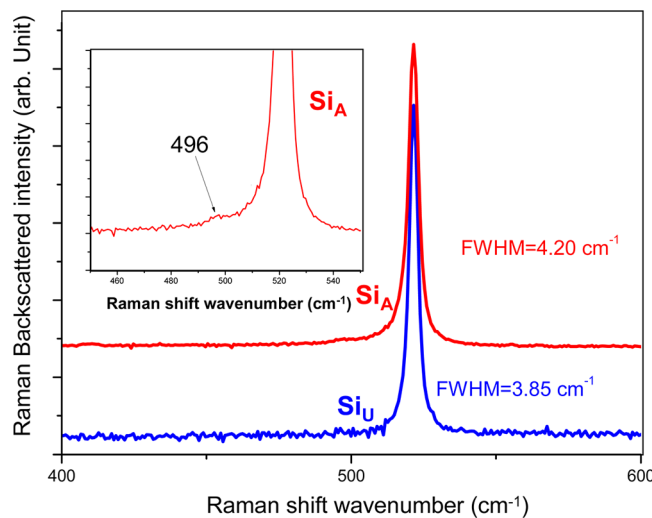


Figure 4. Raman spectra excited at 488 nm (100 μW on about 1 μm^2) of Si_{A} (red) and Si_{U} (blue).

frequency conductivity (for $\nu > 10^7$ Hz) is the same for Si_{U} and Si_{Ud} and is thus intrinsic to the particle bulk. The conductivity of the core of the particles is about 10⁻³ S·m⁻¹ for Si_{U} and Si_{Ud} . The low-frequency conductivity is lower for Si_{Ud} compared to Si_{U} . This is indicative of a more resistive oxidized surface layer and in agreement with the idea of a thicker oxide layer for Si_{Ud} than for Si_{U} . There is about 1 order of magnitude decrease in the conductivity associated with the silicon oxide layer. Same kind of measurements were also recorded on a Si_{A} sample, however, as the particle size and distribution is not the same as for the two other materials, the comparison cannot be easily made. Nevertheless, this Si powder shows same kind of behavior (see Figure S3 in the Supporting Information).

Description of Si–OH, Si–H, and Si–O–Si Bonds by Infrared Spectrometry. In Figure 6 are presented infrared diffuse reflectance spectra of the Si_{A} and Si_{U} powders, between 5500 and 400 cm⁻¹. These spectra were obtained under a low relative humidity smaller than 2%. The large wavenumber range allowed us to follow within the same measurement five spectral regions. (i) The spectral range 4800–5350 cm⁻¹ characterizes the combination ν_2 (bending mode of water molecules) + ν_1 or ν_3 (respectively, the symmetric and the asymmetric stretching modes) of water molecules.⁴² The physisorbed water molecules can be studied separately because this range is fairly isolated from the silica absorptions. The ν_2 mode (bending or δ mode) of the water molecule has been used in the past to determine the quantity of adsorbed water on silica sample. However, the use of this absorption is made difficult by the absorptions of combination and overtone of network silica modes between 1500 and 1850 cm⁻¹. In our case, since the spectra between 4800 and 5400 are totally flat, Figure 6a shows clearly that the water content is very small, as a consequence of the dry atmosphere in the measuring cell. (ii) The region between 3800 and 3000 cm⁻¹ (Figure 6c) corresponds to the fundamental stretching modes of hydroxyl groups. When the content of the physisorbed water is not controlled, this range gathers the hydroxyl groups of water molecules and the hydroxyl groups of the silanol groups. Here, the quantity of water is very low. Then the profile recorded between 3000 and 3800 cm⁻¹ displays the absorption of silanols of the Si powders. It is known that hydrogen bonding decreases the characteristic wavenumber of the stretching ν_{OH} ; but also it increases the

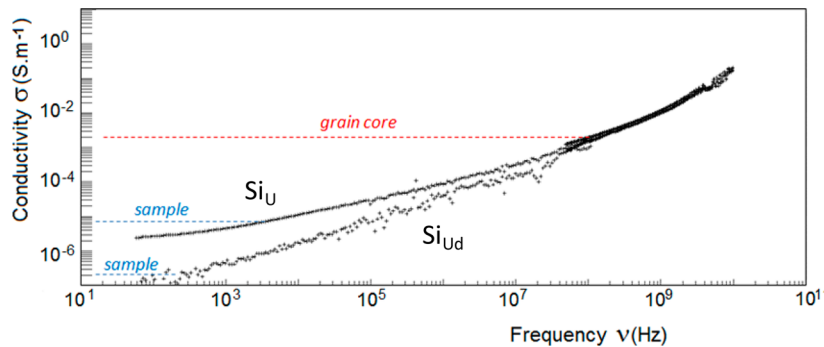


Figure 5. Real parts of the conductivity σ vs frequency for two samples Si_U and Si_{Ud} at 300 K.

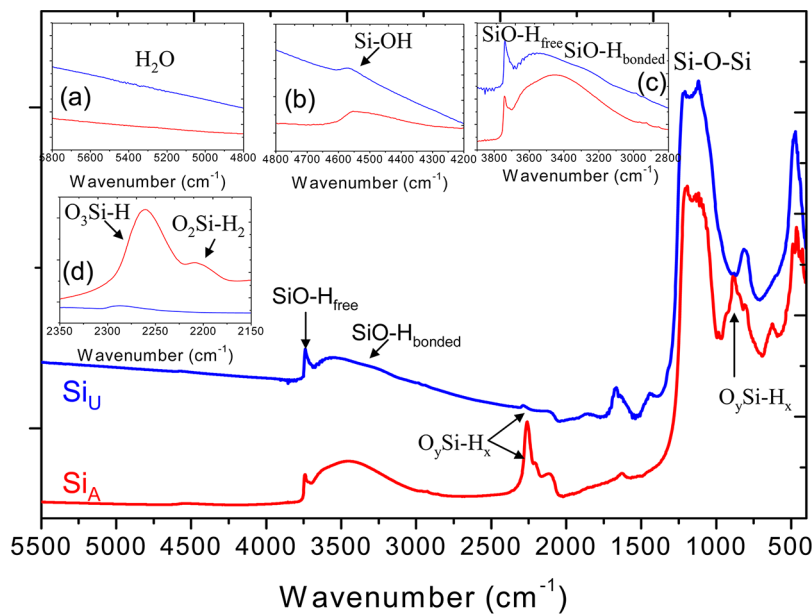


Figure 6. Diffuse infrared reflectance spectra of the sample Si_A (red spectrum) and the sample Si_U (blue spectrum). The spectra were recorded under a relative humidity smaller than 2%. Four zooms are displayed, the $(\delta + \nu)$ combination of (a) water vibration region, (b) the combination of silanol vibrations, (c) the spectral range of the fundamental stretching vibrations of hydroxyl groups (water and silanols), and (d) the range of the fundamental stretching vibrations of $\text{Si}-\text{H}$ groups.

intensity of the corresponding middle infrared transition. Thus, the recorded absorbance, in this range, may be assumed to be, in a first approximation, the result of the “multiplication” of the distribution of silanols by a spectral function strongly decreasing with the wavenumber.⁴³ To reach the true distribution of the hydroxyl groups, the MIR spectrum could be divided by one function $B(\nu)$ representative of the variation with the hydrogen bonds of the square of the absorption transition moment. From a study of weak hydrogen bonds in the liquid phase, the derivative of the dipole moment could be related to the wavenumber by a linear relation.⁴⁴ The function $B(\nu)$ may then be written as $B(\nu) = (6462 - 1.687\nu)^2$. Consequently, the true distribution could be obtained by multiplying the MIR spectrum by the ratio $B(3747)/B(\nu)$. This approach may be applied to amorphous silica samples⁴⁴ and crystalline layered silicate samples.⁴⁵ It would however be better to have a straightforward experimental observation of the OH distribution. In fact, it is also known that the NIR absorbance is weakly dependent on the H-bond effects.^{46,47} (iii) Therefore, we have favored the use of the range between 4800 and 4200 cm^{-1} (Figure 6b), which corresponds to the combination (stretching + angle deformation) of the $\text{Si}-\text{O}-\text{H}$, to obtain a

direct display of the SiOH group distribution, both quantitatively and qualitatively. The absolute quantity has been obtained via a calibration method using parallel ATG measurements (see the next section), while the qualitative description has been obtained by an analysis of the characteristic wavenumber of silanol groups. (iv) The fourth interesting range (Figure 6d) corresponds to the stretching modes of the $\text{Si}-\text{H}$ bonds. In order to explain the various SiH_x bands, an induction effect must be considered through the substitution of more electronegative atoms. This causes the hydride stretching modes to appear at higher frequencies. The range between 2000 and 2150 cm^{-1} thus corresponds to $\text{Si}-\text{Si}-\text{H}_x$ stretching modes, while the range 2150–2350 cm^{-1} corresponds to O_ySiH_x .⁴⁸ Let us note that the spectrum of Si_A sample displays the presence of $\text{O}_3\text{Si}-\text{H}$ and O_2SiH_x contrary to the spectrum of Si_U where the signal is very weak in this range. (v) The last low wavenumber region between 1750 and 400 cm^{-1} allowed us to compare and to follow the $\text{Si}-\text{O}-\text{Si}$ bonds thanks to the double intense band around 1100 cm^{-1} assigned to the TO-LO phonons of silica structures. In the diffuse reflectance mode it is not easy to compare the integrated intensity of this double component to deduce a comparative thickness between the

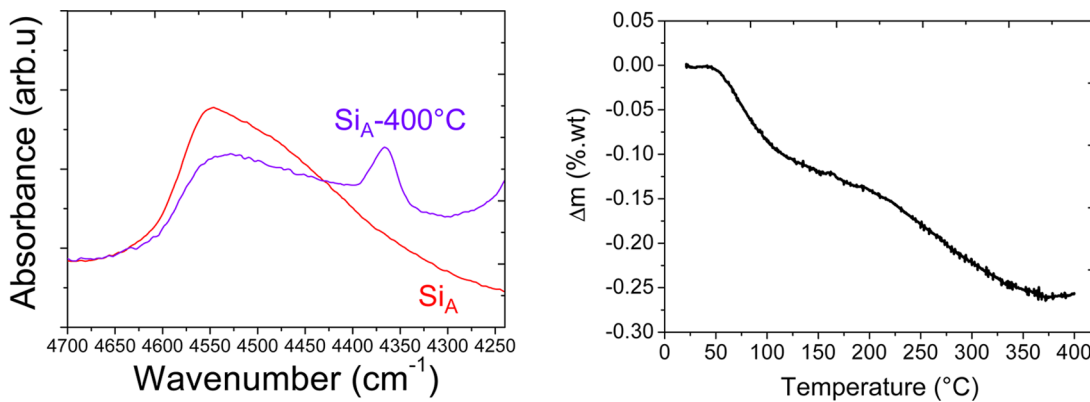


Figure 7. Evolution of the near-infrared spectrum of the sample Si_A (left) and of the mass (right) between room temperature and $400\text{ }^\circ\text{C}$. The noticeable peak at 4380 cm^{-1} is attributed to an organic pollution adsorbed after the thermal treatment. Its contribution was not taken into account in the calculation of n_0 .

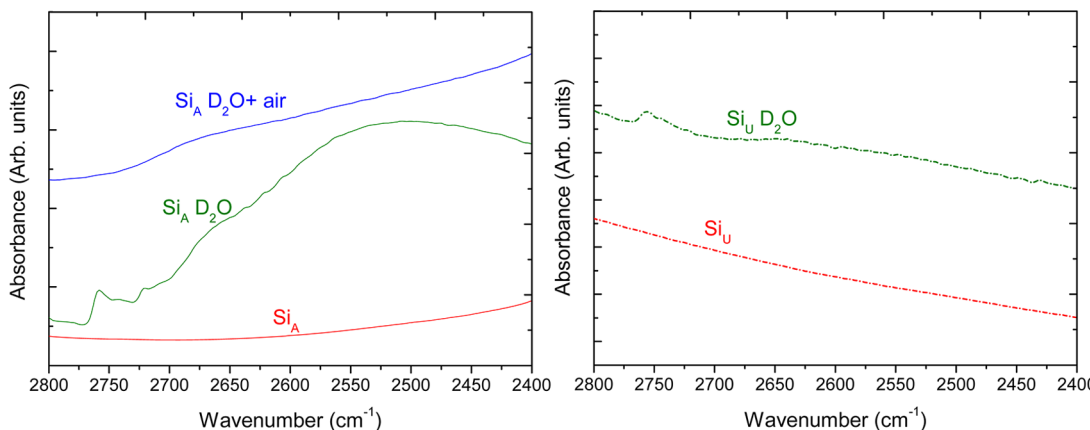


Figure 8. Isotopic frequency of the SiO-D stretch (red) before and (green) after hydrogen–deuterium exchange on (solid) Si_A and (dot) Si_U and (blue) after being placed again in the open air.

oxidation layer of Si_A and Si_U . When a suboxide is assumed in the oxygenated layer, the local environment of the Si atoms in this layer is expected to be nearly identical to that found around Si atoms in SiO_2 , with the exception of Si atoms bounded to hydrogen (i.e., one H atom and three O atom neighbors⁴⁹). It has been shown⁵⁰ that the $[\text{O}]/[\text{Si}]$ ratio r for suboxides roughly scales linearly with the peak frequency of the Si–O bond-stretching absorption band. The value 965 cm^{-1} corresponds to the SiO stretching wavenumber of an O atom in an a-Si:H network and the slope of 50 cm^{-1} ensures that the wavenumber is 1065 cm^{-1} for the SiO_2 end point. The component around 880 cm^{-1} assigned to the O_ySiH_x deformation is absent for the sample Si_U , while it is intense for the sample Si_A , in agreement with the observation made for the Si–H stretching range (Figure 6d).

Determination of Silanols Density. As previously discussed, the NIR absorbance is weakly dependent on the H-bond effects. In Figure 7, the evolution of distribution of the silanol groups after a thermal treatment under nitrogen is illustrated by near-infrared absorption spectra and TGA measurements. The mass of the sample at $100\text{ }^\circ\text{C}$ corresponds to a fully dehydrated sample. Above $100\text{ }^\circ\text{C}$, the weight loss is due to formation of siloxanes group and elimination of water following this reaction: $2\text{SiOH} \rightarrow \text{Si}-\text{O}-\text{Si} + \text{H}_2\text{O}$. We calibrated the decrease of the infrared integrated band, assigned to the Si–OH combined modes, with the quantity of silanol groups lost as measured by TGA. In order to avoid an artifact

with the desorption of the physisorbed water, we have used only the temperature range between 100 and $400\text{ }^\circ\text{C}$. Then we defined the factor of proportionality, P , between the decrease of the experimental integrated IR intensity, ΔI , and the mass loss, Δm , that is, the loss of silanol groups between 100 and $400\text{ }^\circ\text{C}$. ΔI is the difference of integrated intensities of DRIFT spectra from 4700 to 4300 cm^{-1} . P is given by the following relation:

$$P = \frac{\Delta m \times N}{M_{\text{H}_2\text{O}} \times m_{\text{Si}_{\text{sample}}} \times S_{\text{BET}} \times \Delta I} \quad (1)$$

where N is the Avogadro number ($6.02 \times 10^{23}\text{ mol}^{-1}$), $M_{\text{H}_2\text{O}}$ is the H_2O molecular weight (in g mol^{-1}), m_{Si} is the silicon mass analyzed by TGA (in g), and S_{BET} is the specific area (in $\text{m}^2 \cdot \text{g}^{-1}$). This proportionality coefficient allowed us to retrieve the initial specific content, n_0 of silanol groups from

$$n_0 = P \times \int_{4300\text{ cm}^{-1}}^{4700\text{ cm}^{-1}} \text{DRIFT}(\text{Si}_A, 25^\circ\text{C}) \quad (2)$$

where the second term on the right-hand of the equation is the integrated intensity between 4700 and 4300 cm^{-1} . With such a method, we found that the values are 4.9 and 2.7 OH silanols per nanometer square for Si_A and Si_U , respectively. All these silanol groups are easily chemically accessible as proven by the deuteration experiments (Figure 8) where the contact with a D_2O vapor is sufficient to exchange H atoms by D atoms on all these silanol groups. Interestingly, the analysis of the O_ySiH_x

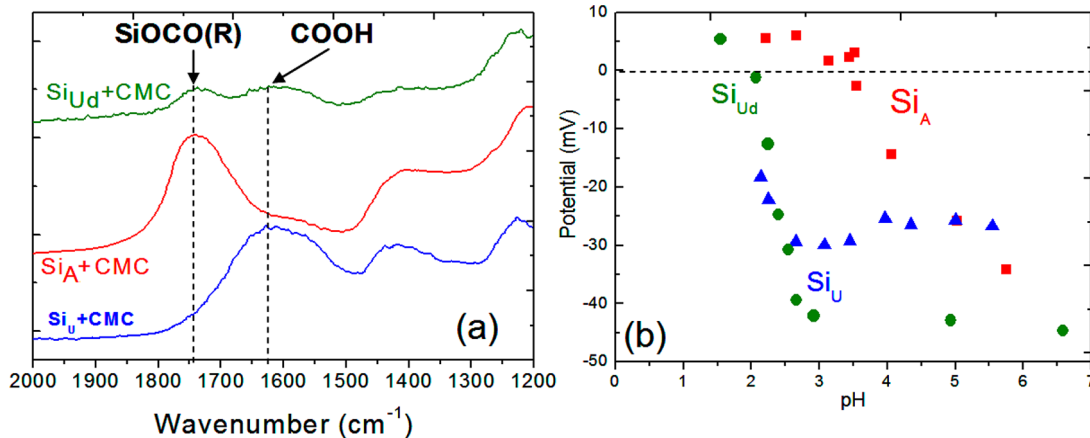


Figure 9. (a) DRIFT MIR spectra of (blue) Si_U, (red) Si_{Ud}, and (red) Si_A after contact with a solution of CMC-acid buffer. (b) Zeta potential vs pH of (blue) Si_U, (green) Si_{Ud}, and (red) Si_A samples.

bands shows that these groups are much less reactive or are not chemically accessible since they were not exchanged in the deuteration experiments (see Figure S4 in the Supporting Information).

In summary, from TEM-EELS and Raman measurements, we have demonstrated that there is a very thin layer of silicon suboxide at the surface of Si_U. Conversely, there is a very well-defined SiO₂ layer (2 nm) at the surface of Si_A. From DRIFT spectroscopy coupled with ATG, we were able to quantify the number of OH per nm². The density of silanol group in Si_A is very close to that found in silica of cristobalite (4.9 OH·nm⁻²), whereas it is significantly lower for Si_U. The latter material was modified through an oxidation treatment (see experimental section) to form at its surface a well-defined SiO₂ layer, as checked by TEM-EELS, Raman and DRIFT spectroscopies (not shown here). The electrochemical performance is different between these three nanometric silicon materials (Si_U, Si_{Ud}, and Si_A), with a better reversibility and longer cycle life for the electrodes based on Si_{Ud} and Si_A (Figure 1), that is, with a well-defined SiO₂ surface layer.

Analysis of the Surface Effect on the Electrode Electrochemical Cycling Stability. In our previous works, we demonstrated better performance (longer cycle life) when the composite electrode was prepared in a buffered acidic aqueous medium rather than in pure water, since the former condition favors the grafting of CMC to Si particles through ester like bonds.¹⁴ The better performance can be assigned to improved mechanical strength of the composite electrode thanks to the formation of stronger and more resilient CMC bridges between the Si particles,^{15,51} when a covalent bonding occurs between the binder and the active material. As a result, the whole electrode architecture shows better capability to sustain the volume variations of the silicon particles upon alloying (dealloying) with lithium. Here, we may wonder if the initial surface of the silicon nanopowder could influence the CMC grafting.

DRIFT spectroscopy was used to analyze the occurrence of esterification of the SiOH groups with the COOH groups of CMC in the composite electrodes. The DRIFT spectra of Si_A-CMC, Si_U-CMC, and Si_{Ud}-CMC composites prepared in pH = 3 buffered solution, dried, further washed with water, and dried again, are shown in Figure 9a. The peak for the Si_U-CMC and Si_{Ud}-CMC composites centered at 1630 cm⁻¹ can be assigned to the stretching band of the carboxyl group of CMC. Almost

80% of this peak disappears for Si_A-CMC, leaving the place to a new peak at 1740 cm⁻¹ that is characteristic of an ester-like bond SiOC(O)R, indicating that CMC has been extensively grafted onto the surface of Si_A particles.¹³ In the case of Si_{Ud}-CMC, the comparison of the peaks at 1630 and at 1740 cm⁻¹ suggests that about half of the COOH groups have been grafted onto the surface of Si_{Ud} to form ester bonds. Contrarily, in the case of Si_U-CMC, there is no peak at 1740 cm⁻¹, demonstrating that little (if any) grafting occurred between Si_U and CMC. The variation of the zeta potential versus pH is presented in Figure 9b. An isoelectric point (IEP) corresponding to a pH of about 3.5 and 2.2 was observed for the Si_A and Si_{Ud}, respectively, while the electrical charge is always negative for Si_U. On the other hand, buffering the slurry allows neutralizing the major part of the COO⁻ into COOH groups. Then, at pH = 3, the neutrality of the Si_A surface is favorable to the CMC binder adsorption onto the silicon particles in the electrode slurry and the formation of hydrogen bonds between the SiOH and COOH groups. After drying and water removal, these hydrogen bonds are transformed at high temperature into ester bonds due to spatial proximity of the SiOH and COOH groups engaged in hydrogen bonds on the Si_A surface. On the contrary, we see here that the stoichiometric oxide layer at the surface of Si_U shows a negative charge at pH = 3 and up to pH = 2. Then we may infer from the zeta potential measurements that a reason for the lack of grafting between CMC and Si_U is that few or no SiOH-COOH hydrogen bonds could be formed upon drying. Si_{Ud} shows an intermediate behavior as a consequence of its IEP value of 2. Upon drying, the pH of the electrode slurry must decrease as the citric acid concentrates, allowing the formation of hydrogen bonds and the subsequent esterification reaction. The grafting of the CMC binder to the surface of the active mass results in improved adhesion between the Si particles in the composite electrode, better reversibility of the lithium alloying/dealloying reaction and thus longer cycle life.^{14,15} In this paper, we show that it is mandatory for the grafting reaction to occur that the silicon particles are covered by a well-defined SiO₂ layer.

After having discussed the influence of physical and chemical composition of the silicon particles surface on the grafting of the CMC binder, let us now discuss the impact of the silicon particles surface composition on the SEI formation. The SEI is a result of the reaction of the charged negative electrode with the electrolyte that is thermodynamically unstable at low

potential and basically consists of electrolyte decomposition products.⁷

XPS measurements were done on Si_{U} - and Si_{Ud} -based composite electrodes to investigate the SEI composition after one cycle. Figure 10 shows $\text{Si}_{2\text{p}}$ XPS spectra of Si_{U} and Si_{Ud} .

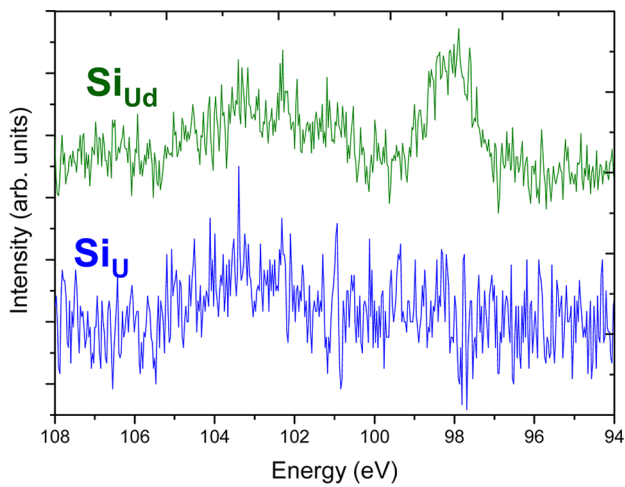


Figure 10. XPS spectra in the region of the $\text{Si}_{2\text{p}}$ peak of (blue) Si_{U} -based and (red) Si_{Ud} -based electrodes after one cycle at the end of charge (delithiation).

based electrodes at the end of the first delithiation. After one cycle, we can see that the peak intensity is very low probably due to the formation of the SEI which is now covering the particles surface. However, the $\text{Si}_{2\text{p}}$ peak intensity is higher for Si_{Ud} than for Si_{U} , suggesting that the SEI is thinner for Si_{Ud} , as expected with the higher Coulombic efficiency, which means a lesser liquid electrolyte degradation, for Si_{Ud} . Moreover, $\text{C}_{1\text{s}}$ spectrum of the Si_{Ud} shows the contribution of the carbon black additive²⁰ while the one of Si_{U} does not (Figure 11), once again in agreement with the occurrence of a thinner SEI in the Si_{Ud} than Si_{U} electrode.⁵² $\text{O}_{1\text{s}}$, $\text{C}_{1\text{s}}$, $\text{F}_{1\text{s}}$, and $\text{P}_{2\text{p}}$ spectra provide insights about the different species formed in the SEI.

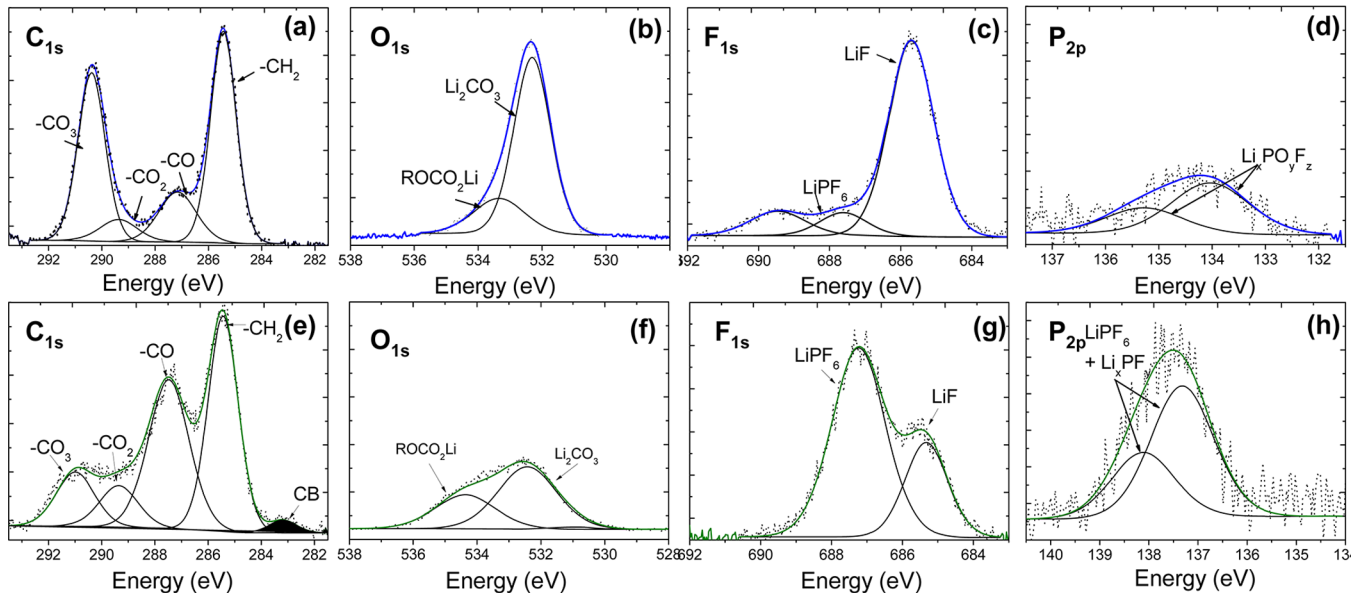


Figure 11. $\text{C}_{1\text{s}}$, $\text{O}_{1\text{s}}$, $\text{F}_{1\text{s}}$, and $\text{P}_{2\text{p}}$ spectra of (blue) Si_{U} and (green) Si_{Ud} -based electrodes after one cycle at the end of charge.

Comparison of the two samples indicates that the chemical composition of the SEI is not similar: amount of LiF, lithium carbonate species (Li_2CO_3) and fluorophosphates ($\text{Li}_x\text{PO}_y\text{F}_z$) are lower at the surface of Si_{Ud} than Si_{U} after one cycle, while the amount of ROCO_2Li is roughly the same in both electrodes. Such results reveal that the LiPF_6 salt is less degraded at the surface of Si_{Ud} particles as LiF, Li_2CO_3 , and $\text{Li}_x\text{PO}_y\text{F}_z$ are typical LiPF_6 degradation products.⁵³ ROCO_2Li species are typical degradation products of carbonate solvents products.⁵⁴

For both samples, Figure 12 shows ^7Li MAS NMR spectra after one cycle at the end of delithiation. The broad resonance

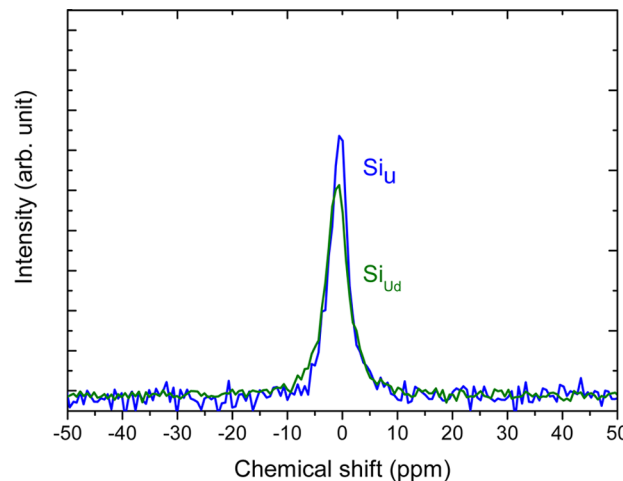


Figure 12. ^7Li NMR spectra recorded at the end of charge after one cycle for (blue) Si_{U} and (green) Si_{Ud} -based electrode.

centered at 0 ppm is usually assigned to diamagnetic lithium and is therefore attributed to lithium present in the SEI (as LiF , Li_2CO_3 , ROCO_2Li , $\text{Li}_x\text{PO}_y\text{F}_z$, ...) and not as trapped Li_xSi alloys in the particles.^{8,55} The normalized intensity of Si_{U} is higher, suggesting that the amount of lithiated degradation products in the SEI is more important for Si_{U} than for Si_{Ud} in agreement

with XPS measurements. Thus, both techniques show that the presence of a thin SiO_2 layer grafted with CMC binder (through the formation of ester like SiOC(O)R bonds) has favorable influence on the first cycle irreversible loss, which is decreased as a consequence of lesser electrolyte degradation. Moreover, it can be noted that the SEI composition is different and is less rich in the lithium salt degradation products when a thin SiO_2 layer is present.

Discussion. At this stage, we should recapitulate the different types of reactions involved in the irreversible capacity losses and pinpoint the differences seen depending on the silicon particles surface composition. From calibration curves and ^7Li NMR integrated intensity (as recently described by our group),^{56,57} we can calculate the absolute amount of lithium (in mol) precipitated at the surface of the electrodes. Furthermore, this quantity can be compared to the number of electron consumed during the first cycle from the irreversible capacity loss given by

$$n_{e^-} = \frac{m_{\text{Si}} \times Q_{\text{loss}} \times 3600}{F} \quad (3)$$

where m_{Si} is the mass of Si in electrode (in g), Q_{loss} is the irreversible capacity (in $\text{mAh}\cdot\text{g}^{-1}$), and F is the Faraday constant ($96489 \text{ C}\cdot\text{mol}^{-1}$). Both quantities are given in Table 2

Table 2. Number of Electrons Lost Calculated from Irreversible Capacity and Number of Lithium Lost in SEI at the Surface of Electrode Calculated from ^7Li NMR for Both Samples

	No. of electrons lost (from irreversible capacity) (mmol/g)	No. of Li lost in SEI (from NMR) (mmol/g)
Si_{U}	17.0	1.3 ± 0.3
Si_{Ud}	13.9	0.9 ± 0.2

for Si_{U} and Si_{Ud} , which shows that the number of lithium involved in the formation of the SEI is rather negligible for both materials compared to the large amount of electrons consumed in irreversible capacity. This result is in agreement with recent

studies from Etacheri et al.⁵⁸ that suggest most of the electrons accounting for the irreversible capacity loss are consumed in the formation of organic byproducts of the degradation of the electrolyte solvents rather than the salt. Furthermore, by ^{13}C NMR⁵⁷ we demonstrated that a significant part of the irreversible capacity loss is due to the degradation of the carbonate solvents with the formation of nonlithiated carbon species as oligomers or polymers such as polycarbonates, which precipitate on the active material.^{9,59}

With respect to the SEI species containing Li ions, identified here by XPS, LiF , and $\text{Li}_x\text{PO}_y\text{F}_z$ species are typical salt degradation products, and Li_2CO_3 and ROCO_2Li species are typical solvent degradation products. In complement, Philippe et al.²⁰ gave strong evidence that the surface SiO_2 layer reacts to form Li_2O and lithium silicate Li_4SiO_4 according to $\text{SiO}_2 + 4\text{Li}^+ + 4e^- \rightarrow \text{Si} + 2\text{Li}_2\text{O}$ and to $2\text{SiO}_2 + 4\text{Li}^+ + 4e^- \rightarrow \text{Si} + \text{Li}_4\text{SiO}_4$. Since we have not detected Li_2O by XPS, we may calculate the number of electron loss, n_{e^-} , due to formation of a possible lithium silicate Li_4SiO_4 :

$$n_{e^-} = 2 \times \left[\frac{4\pi}{3} (R^3 - r_0^3) \frac{\rho_{\text{SiO}_2}}{M_{\text{SiO}_2}} \right] \times \left[\frac{m}{\rho_{\text{Si}}} \left(\frac{3}{4\pi R^3} \right) \right] \quad (4)$$

where the first term gives the number of mole of SiO_2 per silicon particle and the second term gives the number of silicon particles in the composite electrode. The factor 2 comes from the ratio 1 SiO_2 for $2e^-$ in $2\text{SiO}_2 + 4\text{Li}^+ + 4e^- \rightarrow \text{Si} + \text{Li}_4\text{SiO}_4$. ρ_{SiO_2} and ρ_{Si} are the density of silica ($2.65 \text{ g}\cdot\text{cm}^{-3}$) and silicon ($2.33 \text{ g}\cdot\text{cm}^{-3}$), respectively, m is the mass of silicon in the electrode (1 mg), M_{SiO_2} is the molecular weight of silica. R is the radius of silicon particles (50 nm) and assuming the thickness of silicon oxide to be close to 1.5 nm, we have $r_0 = 48.5$ nm, which is the difference between the radius of silicon particle and the silicon oxide layer. The result obtained is equal to $1.1 \mu\text{mol}$ of electrons. This value is of the same order as the amount of lithium measured by ^7Li NMR for Si_{Ud} . This complementary amount of electrons, which is expected to be

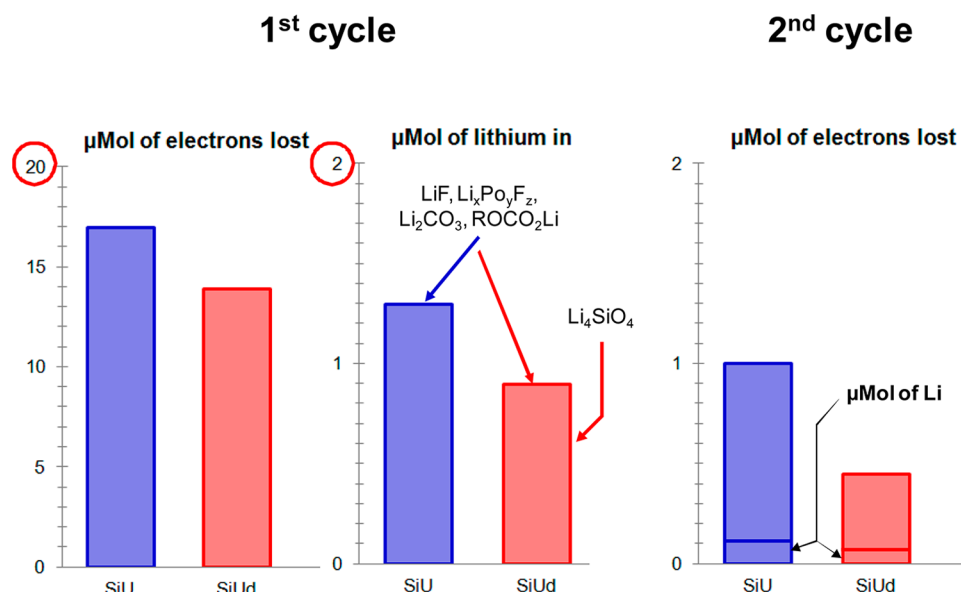


Figure 13. Number of μmol of electrons (as determined from irreversible capacity) and lithium lost (as determined by ^7Li NMR) for Si_{U} and Si_{Ud} at the 1st and 2nd cycle. With respect to the lithium species, we considered no Li_4SiO_4 species formed on Si_{U} as their quantity is likely negligible.

involved in the formation of a lithium silicate phase, is not significant to explain the first cycle capacity loss.

In Figure 13 is recapped our estimations of the amounts of electrons lost at the first and second cycles and the amounts of lithium lost in different species (lithium silicates, lithium salt degradation products LiF and $\text{Li}_x\text{PO}_y\text{F}_z$, and solvent degradation products Li_2CO_3 and ROCO_2Li). With respect to silicates, we considered a SiO_2 layer of 1.5 nm for Si_{Ud} and no SiO_2 layer for Si_{U} . Figure 13 clearly shows again that the presence of a thin SiO_2 layer is favorable to the formation of a thinner SEI. We note that the amount of lithium salt degradation species is dramatically decreased (from 1.3 to nearly 0 μmol), which can be attributed to decreased reactivity of the particles surface by the neutralization of the fairly reactive and Lewis acid SiOH groups through the formation of ester bond with the CMC binder. However, the major contribution to the first cycle and cumulative irreversible capacity loss is due to the electrolyte solvent degradation and formation of polycarbonate.

The grafted SiOC(O)CMC layer also plays a favorable role by decreasing the extent of electrolyte solvent reduction in the following cycles (Table 1). Nadimpalli et al.⁶⁰ measured the absolute capacity loss due to SEI layer formation on naked silicon thin film (with no binder adsorbed or grafted to its surface) to be in the range 0.018 and 0.028 $\text{mAh}\cdot\text{cm}^{-2}$. In the case of the Si_{U} - and Si_{Ud} -based composite electrodes, the capacity loss per unit surface area of Si plus CB powder is 0.0022 and 0.0020 $\text{mAh}\cdot\text{cm}^{-2}$ for Si_{U} and Si_{Ud} respectively (by taking into account their BET surface area). This represents less than 10% of the value found for a naked silicon thin film. This observation shows that in both cases, the presence of an adsorbed (Si_{U}) or grafted (Si_{Ud}) CMC layer strongly reduces the first cycle irreversible loss. Nevertheless, the grafted case is clearly more favorable after the first cycle. More adhesive interparticle contacts likely allows a more reversible breathing of the composite electrode architecture upon lithium alloying/dealloying with less sliding and displacement of the particles and thus less scrapping of the SEI layer upon the redistribution of contacts between the particles.² Thus, the presence of a SiO_2 layer, although contributing to the first cycle irreversible capacity loss through the formation of Li_4SiO_4 ,²⁰ is beneficial and mandatory for a good cyclability of the Si-based composite electrode, as observed in Figure 1, in contradiction with common belief that no SiO_2 layer at the surface of silicon nanoparticles makes a better material for the lithium-ion battery application.^{21,23}

CONCLUSION

A pluri-disciplinary approach and a combination of techniques were here used to finely describe the surface of silicon nanoparticles used as active material in negative composite electrodes for lithium batteries. Although the surface of silicon particles is playing a major role in the electrochemical performance, it has rarely been characterized in depth. TEM-EELS and Raman revealed the presence of a very thin layer of silicon suboxide at the surface of Si_{U} . Conversely, there is a very well-defined SiO_2 layer (2 nm) at the surface of Si_{A} . From DRIFT spectroscopy coupled with ATG, we were able to quantify the number of SiOH per nm^2 . The density of silanol group in Si_{A} is very close to that found in silica of cristobalite (4.9 $\text{OH}\cdot\text{nm}^{-2}$), whereas it is significantly lower for Si_{U} . The latter material was modified (Si_{Ud}) to form at its surface a well-defined SiO_2 layer. BDS shows the SiO_2 layer increases the resistivity of the silicon powder. Moreover, the presence of a

SiO_2 layer, although contributing to the first cycle irreversible capacity loss through the formation of lithium silicate, is very beneficial and mandatory for a good cyclability of the Si-based composite electrode. Indeed, the electrochemical performance of Si_{A} and Si_{Ud} are significantly superior to Si_{U} . The latter shows higher irreversible losses and lower cycle life. The grafting of the CMC binder at the surface of both Si_{A} and Si_{Ud} was demonstrated by DRIFT. The occurrence of grafting is possible when a well-defined SiO_2 layer is covering the surface of the silicon particles as a consequence of favorable zeta potential and molecular interactions in the electrode slurry with the CMC chains. The grafting of the CMC binder increases the mechanical strength of the composite electrode and its ability to reversibly sustain the volume variations of the silicon particles upon (de)alloying with lithium. Furthermore, the surface reactivity of silicon particles toward the lithium salt of the electrolyte is decreased thanks to the disappearance of the SiOH involved in the grafting reaction.

We have performed other EELS experiments with smaller size probes (<1 nm), DRIFT analysis and electrochemical measurements on a series of Si_{Ud} with varying oxide layers, which confirm the results presented here. We found no influence of the oxide layer thickness on the cyclability of silicon-based composite electrodes with the electrode formulation used here. As long as a well-defined oxide is present at the surface of the particles and allows the grafting of the CMC binder, a much better cyclability is observed compared to that of Si_{U} , which has no well-defined oxide layer at its surface.⁶¹

ASSOCIATED CONTENT

S Supporting Information

Figure S1: SEM observation of a Si/CMC/CB composite electrode before cycling. Figure S2: XRD pattern of the (red) Si_{A} and (blue) Si_{U} nanopowders. Figure S3: Real part of the conductivity σ vs frequency for samples Si_{A} at 300 K. Figure S4: DRIFT spectra on the range of the fundamental stretching vibrations of Si-H groups (red) before and (green) after hydrogen-deuterium exchange on Si_{A} and (blue) after being placed again in the open air. This material is available free of charge via the Internet at <http://pubs.acs.org>.

AUTHOR INFORMATION

Corresponding Author

*E-mail: bernard.lestriez@cnrs-imn.fr.

Notes

The authors declare no competing financial interest.

ACKNOWLEDGMENTS

XPS measurements were achieved in the Nanocharacterization Center (PFNC) at Minatec Campus, CEA-Grenoble.

REFERENCES

- (1) Beaulieu, L. Y.; Eberman, K. W.; Turner, R. L.; Krause, L. J.; Dahn, J. R. Colossal Reversible Volume Changes in Lithium Alloys. *Electrochim. Solid-State Lett.* **2001**, *4*, A137–A140.
- (2) Nguyen, B. P. N.; Gaubicher, J.; Lestriez, B. Analogy between Electrochemical Behaviour of Thick Silicon Granular Electrodes for Lithium Batteries and Fine Soils Micromechanics. *Electrochim. Acta* **2014**, *120*, 319–326.
- (3) Liu, W.; Yang, M.; Wu, H.; Chiao, S. M.; Wu, N. Enhanced Cycle Life of Si Anode for Li-Ion Batteries by Using Modified Elastomeric Binder. *Electrochim. Solid-State Lett.* **2005**, *8*, A100–A103.

- (4) Ryu, J. H.; Kim, J. W.; Sung, Y.; Oh, S. M. Failure Modes of Silicon Powder Negative Electrode in Lithium Secondary Batteries. *Electrochim. Solid-State Lett.* **2004**, *7*, A306–A309.
- (5) Park, S.; Kim, T.; Oh, S. M. Electrochemical Dilatometry Study on Si-Embedded Carbon Nanotube Powder Electrodes. *Electrochim. Solid-State Lett.* **2007**, *10*, A142–A145.
- (6) Reyter, D.; Rousselot, S.; Mazouzi, D.; Gauthier, M.; Moreau, P.; Lestriez, B.; Guyomard, D.; Roué, L. An Electrochemically Roughened Cu Current Collector for Si-Based Electrode in Li-Ion Batteries. *J. Power Sources* **2013**, *239*, 308–314.
- (7) Winter, M. The Solid Electrolyte Interphase: The Most Important and the Least Understood Solid Electrolyte in Rechargeable Li Batteries. *Z. Phys. Chem.* **2009**, *223*, 1395–1406.
- (8) Oumella, Y.; Delpuech, N.; Mazouzi, D.; Dupré, N.; Gaubicher, J.; Moreau, P.; Soudan, P.; Lestriez, B.; Guyomard, D. The Failure Mechanism of Nano-Sized Si-Based Negative Electrodes for Lithium Ion Batteries. *J. Mater. Chem.* **2011**, *21*, 6201–6208.
- (9) Mazouzi, D.; Delpuech, N.; Oumella, Y.; Gauthier, M.; Cerbelaud, M.; Gaubicher, J.; Dupré, N.; Moreau, P.; Guyomard, D.; Roué, L.; et al. New Insights into the Silicon-Based Electrode's Irreversibility Along Cycle Life Through Simple Gravimetric Method. *J. Power Sources* **2012**, *220*, 180–184.
- (10) Vidal, A.; Balard, H.; Papirer, E.; Czemichowski, M.; Erre, R.; Levitz, P.; Damme, H. V.; Gallas, J.; Hemedy, J.; Lavalle, J.; et al. Hydroxyls of Silica Powders. *Adv. Colloid Interface Sci.* **1990**, *33*, 91.
- (11) Bridel, J. S.; Azais, T.; Morcrette, M.; Tarascon, J. M.; Larcher, D. In Situ Observation and Long-Term Reactivity of Si/C/CMC Composites Electrodes for Li-ion Batteries. *J. Electrochim. Soc.* **2011**, *158*, A750–A759.
- (12) Bridel, J. S.; Azais, T.; Morcrette, M.; Tarascon, J. M.; Larcher, D. Key Parameters Governing the Reversibility of Si/Carbon/CMC Electrodes for Li-ion Batteries. *Chem. Mater.* **2009**, *22*, 1229–1241.
- (13) Hochgatterer, N. S.; Schweiger, M. R.; Koller, S.; Raimann, P. R.; Wohrle, T.; Wurm, C.; Winter, M. Silicon/Graphite Composite Electrodes for High-Capacity Anodes: Influence of Binder Chemistry on Cycling Stability. *Electrochim. Solid-State Lett.* **2008**, *11*, A76–A80.
- (14) Mazouzi, D.; Lestriez, B.; Roué, L.; Guyomard, D. Silicon Composite Electrode with High Capacity and Long Cycle Life. *Electrochim. Solid-State Lett.* **2009**, *12*, A215–A218.
- (15) Maver, U.; Znidarsic, A.; Gaberscek, M. An Attempt to Use Atomic Force Microscopy for Determination of Bond Type in Lithium Battery Electrodes. *J. Mater. Chem.* **2011**, *21*, 4071–4075.
- (16) Koo, B.; Kim, H.; Cho, Y.; Lee, K. T.; Choi, N.; Cho, J. A Highly Cross-Linked Polymeric Binder for High-Performance Silicon Negative Electrodes in Lithium Ion Batteries. *Angew. Chem., Int. Ed.* **2012**, *51*, 8762–8767.
- (17) Ding, N.; Xu, J.; Yao, Y.; Wegner, G.; Lieberwirth, I.; Chen, C. Improvement of Cyclability of Si as Anode for Li-Ion Batteries. *J. Power Sources* **2009**, *192*, 644–651.
- (18) Song, S.; Baek, S. Silane-Derived SEI Stabilization on Thin-Film Electrodes of Nanocrystalline Si for Lithium Batteries. *Electrochim. Solid-State Lett.* **2009**, *12* (2), A23–A27.
- (19) Xu, K.; Von Cresce, A. Interfacing Electrolytes with Electrodes in Li Ion Batteries. *J. Mater. Chem.* **2011**, *21*, 9849–9864.
- (20) Philippe, B.; Dedryvère, R.; Allouche, J.; Lindgren, F.; Gorgoi, M.; Rensmo, H.; Gonbeau, D.; Edstrom, K. Nanosilicon Electrodes for Lithium-Ion Batteries: Interfacial Mechanisms Studied by Hard and Soft X-ray Photoelectron Spectroscopy. *Chem. Mater.* **2012**, *24*, 1107–1115.
- (21) Xun, S.; Song, X.; Grass, M. E.; Roseguo, D. K.; Liu, Z.; Battaglia, V. S.; Liu, G. Improved Initial Performance of Si Nanoparticles by Surface Oxide Reduction for Lithium-Ion Battery Application. *Electrochim. Solid-State Lett.* **2011**, *14*, A61–A63.
- (22) Xun, S.; Song, X.; Wang, L.; Grass, M. E.; Liu, Z.; Battaglia, V. S.; Liu, G. The Effects of Native Oxide Surface Layer on the Electrochemical Performance of Si Nanoparticle-Based Electrodes. *J. Electrochim. Soc.* **2011**, *158*, A1260–A1266.
- (23) Yu, B.; Hwa, Y.; Park, C.; Kim, J.; Sohn, H. Effect of Oxide Layer Thickness to Nano-Si Anode for Li-Ion Batteries. *RSC Adv.* **2013**, *3*, 9408–9413.
- (24) Profatilova, I. A.; Stock, C.; Schmitz, A.; Passerini, S.; Winter, M. Enhanced Thermal Stability of a Lithiated Nano-Silicon Electrode by Fluoroethylene Carbonate and Vinylene Carbonate. *J. Power Sources* **2013**, *222*, 140–149.
- (25) Dalavi, S.; Guduru, P.; Brett, L. Performance Enhancing Electrolyte Additives for Lithium Ion Batteries with Silicon Anodes. *J. Electrochim. Soc.* **2012**, *159*, A642–A646.
- (26) Markevich, E.; Fridman, K.; Sharabi, R.; Elazari, R.; Salitra, G.; Gottlieb, H. E.; Gershinsky, G.; Garsuch, A.; Semrau, G.; Schmidt, M. A.; et al. Amorphous Columnar Silicon Anodes for Advanced High Voltage Lithium Ion Full Cells: Dominant Factors Governing Cycling Performance. *J. Electrochim. Soc.* **2013**, *160*, A1824–A1833.
- (27) Driesen, K.; Nelis, D.; Put, S.; Scoyer, J. Submicron Sized Silicon Powder with Low Oxygen Content. U.S. Patent WO 2012/000858 A1, 2012.
- (28) Grausem, J.; Humbert, B.; Spajer, M.; Courjon, D.; Burneau, A.; Oswalt, J. Near-Field Raman Spectroscopy. *J. Raman Spectrosc.* **1999**, *30*, 833–840.
- (29) Miska, P.; Dossot, M.; Nguyen, T. D.; Grun, M.; Rinnert, H.; Vergnat, M.; Humbert, B. Embedded Silicon Nanocrystals Studied by Photoluminescence and Raman Spectroscopies: Exciton and Phonon Confinement Effects. *J. Phys. Chem. C* **2010**, *114*, 17344–17349.
- (30) Fallon, P.; Walsh, C. A. PEELS Programme; University of Cambridge: England, 1996.
- (31) Belhadj-Tahar, N. E.; Fourrier-Lamer, A. Broad-Band Analysis of a Coaxial Discontinuity used for Dielectric Measurements. *IEEE Trans. Microwave Theory Tech.* **1986**, *34*, 346.
- (32) Berthumeyrie, S.; Badot, J.; Pereira Ramos, J.; Dubrunfaut, O.; Bach, S.; Vermaut, P. Influence of Lithium Insertion on the Electronic Transport in Electroactive MoO₃ Nanobelts and Classical Powders: Morphological and Particle Size Effects. *J. Phys. Chem. C* **2010**, *114*, 19803.
- (33) Nguyen, B. P. N.; Kumar, N. A.; Gaubicher, J.; Duclairoir, F.; Brousse, T.; Crozier, O.; Dubois, L.; Bidan, G.; Guyomard, D.; Lestriez, B. Nanosilicon-based Thick Negative Composite Electrodes for Lithium Batteries with Graphene as Conductive Additive. *Adv. Energy Mater.* **2013**, *3*, 1351–1357.
- (34) Batson, P. E. Simultaneous STEM Imaging and Electron Energy-Loss Spectroscopy with Atomic-Column Sensitivity. *Nature* **1993**, *366*, 727–728.
- (35) Muller, D.; Sorsch, T.; Moccio, S.; Baumann, F.; Evans, K.; Timp, G. The Electronic Structure at the Atomic Scale of Ultrathin Gate Oxides. *Nature* **1999**, *399*, 758.
- (36) Humbert, B. Estimation of Hydroxyl Density at the Surface of Pyrogenic Silicas by Complementary NMR and Raman Experiments. *J. Non-Cryst. Solids* **1995**, *191*, 29–37.
- (37) Badot, J.; Ligneel, E.; Dubrunfaut, O.; Guyomard, D.; Lestriez, B. A Multiscale Description of the Electronic Transport within the Hierarchical Architecture of a Composite Electrode for Lithium Batteries. *Adv. Funct. Mater.* **2009**, *19*, 2749.
- (38) Badot, J.; Ligneel, E.; Dubrunfaut, O.; Gaubicher, J.; Guyomard, D.; Lestriez, B. Influence of Adsorbed Polar Molecules on the Electronic Transport in a Composite Material Li_{1.1}V₃O₈–PMMA for Lithium Batteries. *Phys. Chem. Chem. Phys.* **2012**, *14*, 9500.
- (39) Seid, K.; Badot, J.; Dubrunfaut, O.; Levasseur, S.; Guyomard, D.; Lestriez, B. Multiscale Electronic Transport Mechanism and True Conductivities in Amorphous Carbon–LiFePO₄ Nanocomposites. *J. Mater. Chem.* **2012**, *22*, 2641.
- (40) Seid, K.; Badot, J.; Dubrunfaut, O.; Levasseur, S.; Guyomard, D.; Lestriez, B. Influence of the Carboxymethyl Cellulose Binder on the Multiscale Electronic Transport in Carbon–LiFePO₄ Nanocomposites. *J. Mater. Chem.* **2012**, *22*, 24057.
- (41) Seid, K.; Badot, J.; Dubrunfaut, O.; Caldes, M.; Stephan, N.; Gautier, L.; Guyomard, D.; Lestriez, B. Multiscale Electronic Transport in a Broadband Dielectric Study from 40 Hz to 10 GHz. *Phys. Chem. Chem. Phys.* **2013**, *15*, 19790–19798.

- (42) Gallas, J. P.; Lavalley, J. C.; Burneau, A.; Barres, O. Comparative Study of the Surface Hydroxyl Groups of Fumed and Precipitated Silicas. 4. Infrared Study of Dehydroxylation by Thermal Treatments. *Langmuir* **1991**, *7*, 1235–1240.
- (43) Carteret, C. Etude par Spectroscopie dans le Proche Infrarouge et Modélisation des Structures de Surface et de l'Hydratation de Silices Amorphe. *Ph.D. Thesis*, University UHP, Nancy 1, 1999.
- (44) Burneau, A.; Barres, O.; Gallas, J. P.; Lavalley, J. C. Comparative Study of the Surface Hydroxyl Groups of Fumed and Precipitated Silicas. 2. Characterization by Infrared Spectroscopy of the Interactions with Water. *Langmuir* **1990**, *6*, 1364–1372.
- (45) Eypert-Blaison, C.; Michot, L. J.; Humbert, B.; Pelletier, M.; Villières, F. Hydration Water and Swelling Behavior of Magadiite. The H^+ , Na^+ , K^+ , Mg^{2+} , and Ca^{2+} Exchanged Forms. *J. Phys. Chem. B* **2001**, *106*, 730–742.
- (46) Burneau, A.; Gallas, J. Hydroxyl Groups on Silica Surfaces. In *The Surface Properties of Silicas*; Legrand, A. P., Ed.; Wiley: New York, 1998.
- (47) Humbert, B.; Burneau, A.; Gallas, J.; Lavalley, J. Origin of the Raman Bands, D1 and D2, in High Surface Area and Vitreous Silicas. *J. Non-Cryst. Solids* **1992**, *143*, 75–83.
- (48) Mawhinney, D. B.; Glass, J. A.; Yates, J. T. FTIR Study of the Oxidation of Porous Silicon. *J. Phys. Chem. B* **1997**, *101*, 1202–1206.
- (49) Tsu, D. V.; Lucovsky, G.; Davidson, B. N. Effects of the Nearest Neighbors and the Alloy Matrix on SiH Stretching Vibrations in the Amorphous SiO_rh ($0 < r < 2$) alloy system. *Phys. Rev. B* **1989**, *40*, 1795–1805.
- (50) Pai, P.; Chao, S.; Takagi, Y.; Lucovsky, G. Infrared Spectroscopic Study of SiOx Films Produced by Plasma Enhanced Chemical Vapor Deposition. *J. Vac. Sci. Technol. A* **1986**, *4*, 689.
- (51) Lestriez, B.; Bahri, S.; Sandu, I.; Roué, L.; Guyomard, D. On the Binding Mechanism of CMC in Si Negative Electrodes for Li-Ion Batteries. *Electrochim. Commun.* **2007**, *9*, 2801–2806.
- (52) Komaba, S.; Okushi, K.; Ozeki, T.; Yui, H.; Katayama, Y.; Miura, T.; Saito, T.; Grault, H. Polyacrylate Modifier for Graphite Anode of Lithium-Ion Batteries. *Electrochim. Solid-State Lett.* **2009**, *12*, A107–A110.
- (53) Aurbach, D. Review of Selected Electrode Solution Interactions which Determine the Performance of Li and Li Ion Batteries. *J. Power Sources* **2000**, *89*, 206–218.
- (54) Lux, S.; Lucas, I.; Pollak, E.; Passerini, S.; Winter, M.; Kostecki, R. The Mechanism of HF Formation in $LiPF_6$ Based Organic Carbonate Electrolytes. *Electrochim. Commun.* **2012**, *14*, 47–50.
- (55) Key, B.; Bhattacharyya, R.; Morcrette, M.; Seznec, V.; Tarascon, J.-M.; Grey, C. P. Real-Time NMR Investigations of Structural Changes in Silicon Electrodes for Lithium-Ion Batteries. *J. Am. Chem. Soc.* **2009**, *131*, 9239–9249.
- (56) Cuisinier, M.; Martin, J. F.; Moreau, P.; Epicier, T.; Kanno, R.; Guyomard, D.; Dupré, N. Quantitative MAS NMR Characterization of the $LiMn_{1/2}Ni_{1/2}O_2$ Electrode/Electrolyte Interphase. *Solid State Nucl. Magn. Reson.* **2012**, *42*, 51–61.
- (57) Delpuech, N.; Dupré, N.; Mazouzi, D.; Gaubicher, J.; Moreau, P.; Bridel, J.; Guyomard, D.; Lestriez, B. Correlation between Irreversible Capacity and Electrolyte Solvents Degradation probed by NMR in Si-Based Negative Electrode of Li-Ion Cell. *Electrochim. Commun.* **2013**, *33*, 72–75.
- (58) Etacheri, V.; Haik, O.; Goffer, Y.; Roberts, G. A.; Stefan, I. C.; Fasching, R.; Aurbach, D. Effect of Fluoroethylene Carbonate (FEC) on the Performance and Surface Chemistry of Si-Nanowire Li-Ion Battery Anodes. *Langmuir* **2012**, *28*, 965.
- (59) Leung, K. Two-Electron Reduction of Ethylene Carbonate: A Quantum Chemistry Re-Examination of Mechanisms. *Chem. Phys. Lett.* **2013**, *568–569*, 1–8.
- (60) Nadimpalli, S. P.; Sethuraman, V. A.; Dalavi, S.; Lucht, B.; Chon, M. J.; Shenoy, V. B.; Guduru, P. R. Quantifying Capacity Loss Due to Solid-Electrolyte-Interphase Layer Formation on Silicon Negative Electrodes in Lithium-Ion Batteries. *J. Power Sources* **2012**, *215*, 145–151.
- (61) Delpuech, N.; et al. Manuscript to be published.